Effects of extracellular matrix rigidity on sonoporation facilitated by targeted microbubbles: Bubble attachment, bubble dynamics, and cell membrane permeabilization

Ning Rong[a], Meiru Zhang[a], Yulin Wang[a], Hao Wu[b], Hui Qi[b], Xing Fu[b], Dachao Li[b], Chunmei Yang[a], Yan Wang[a], Zhenzhen Fan[a,c,*]

[a] Department of Biomedical Engineering, School of Precision Instruments and Opto-Electronics Engineering, Tianjin University, Tianjin 300072, China
[b] State Key Laboratory of Precision Measuring Technology and Instruments, Tianjin University, Tianjin 300072, China
[c] State Key Laboratory of Acoustics, Institute of Acoustics, Chinese Academy of Sciences, Beijing 100190, China

ARTICLE INFO

ABSTRACT

In this study, we investigated the effects of extracellular matrix rigidity, an important physical property of microenvironments regulating cell morphology and functions, on sonoporation facilitated by targeted microbubbles, highlighting the role of microbubbles. We conducted mechanistic studies at the cellular level on physiologically relevant soft and rigid substrates. By developing a unique imaging strategy, we first resolved details of the 3D attachment configurations between targeted microbubbles and cell membrane. High-speed video microscopy then unveiled bubble dynamics driven by a single ultrasound pulse. Finally, we evaluated the cell membrane permeabilization using a small molecule model drug. Our results demonstrate that: (1) stronger targeted microbubble attachment was formed for cells cultured on the rigid substrate, while six different attachment configurations were revealed in total; (2) more violent bubble oscillation was observed for cells cultured on the rigid substrate, while one third of bubbles attached to cells on the soft substrate exhibited deformation shortly after ultrasound was turned off; (3) higher acoustic pressure was needed to permeabilize the cell membrane for cells on the soft substrate, while under the same ultrasound condition, acoustically-activated microbubbles generated larger pores as compared to cells cultured on the soft substrate. The current findings provide new insights to understand the underlying mechanisms of sonoporation in a physiologically relevant context and may be useful for the clinical translation of sonoporation.

1. Introduction

The combination of ultrasound and microbubbles for enhanced intracellular drug delivery, as a non-viral, non-invasive approach, integrates the superior safety profile and focusing ability of ultrasound, rendering this technique great advantages for clinical applications. Because of the large acoustic impedance mismatch between the gas inside the bubbles and the surrounding medium, ultrasound contrast agent microbubbles can generate a rich variety of phenomena when exposed to an ultrasound field, including inertial and stable cavitation [1–5]. The resulting transient and reversible disruption on the cell membrane nearby allows intracellular uptake of exogenous therapeutic agents. Human clinical trials have been reported using ultrasound and microbubbles to enhance the chemotherapeutic treatment of pancreatic cancer [6] and malignant tumors in the digestive system [7]. The accelerating clinical translation arises a stronger desire to elucidate the fundamental mechanisms of this technique in physiologically relevant contexts.

The acoustic activities of microbubbles play an essential role, bridging the ultrasound energy and the endpoint delivery outcomes. Previous work has unveiled how ultrasound parameters [8,9], initial and boundary conditions [10–12], and chemical and physical properties of microbubbles [13,14] affect microbubble cavitation behavior, as well as the bioeffects downstream. Because sonoporation results from the mechanical interaction between microbubbles and cells, the properties of cells should also be taken into consideration. The impact of the cell cycle on sonoporation has been recently reported [15,16]. However, little has been known about the effects of extracellular matrix (ECM) rigidity, an important physical property of the microenvironments regulating cell mechanics and functions, on sonoporation.

* Corresponding author at: Department of Biomedical Engineering, Tianjin University, No. 92 Weijin Road, Nankai District, Tianjin 300072, China.
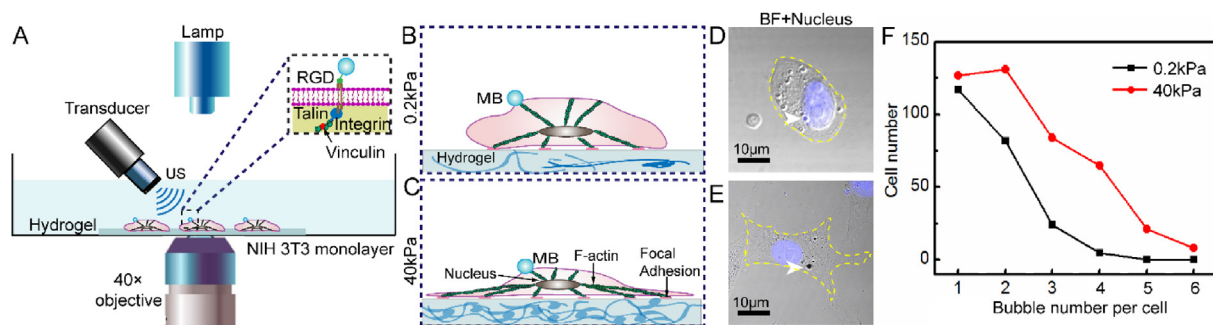 *E-mail address:* zhenzhen.fan@tju.edu.cn (Z. Fan).

Fig. 1. (A) The experimental setup for sonoporation facilitated by targeted microbubbles. Targeted microbubbles were attached to cells via RGD-integrin bindings. Illustrations (B, C) and bright field microscopic images (D, E) for cells cultured on soft and rigid substrates with a targeted microbubble. (F) Cell number with different number of microbubbles attached per cell.

The heterogeneous physical microenvironments across tissues are increasingly recognized as crucial regulators of cell morphology, functions and fate [17,18]. The ECM rigidity alone can regulate cell morphology [19–21], alter cell stiffness [22,23], even promote cancer development [24,25] and direct stem cell lineage commitment [26,27]. The ECM rigidity ranges from < 1 kPa in brain tissue and 10 kPa in muscles to > 100 kPa in bone. What is more noteworthy is that this elasticity range is 6–7 orders of magnitude less than that of the plastics or glass [28], which are the cell culture substrates that were used in almost all in vitro sonoporation mechanistic studies with attached cell lines reported so far [29–31].

Facilitated by the ligands decorated on the shell, targeted microbubbles can select and adhere to diseased cells. This feature of targeted microbubbles not only enables ultrasound molecular imaging, but further empowers the targeting ability of drug delivery using ultrasound-excited microbubbles. The attachment between targeted microbubbles and the cell membrane serves as the initial condition for bubble oscillation subjected to an ultrasound field, while the physical properties of the cell serve as the boundary condition. Since the receptor expression and the physical properties of the cell are all regulated by ECM rigidity [21,22], we speculate that compared with sonoporation facilitated by free bubbles, sonoporation facilitated by targeted microbubbles would be more profoundly impacted by the ECM rigidity.

This study is designed to investigate the influence of ECM rigidity on sonoporation facilitated by targeted microbubbles, highlighting the role of microbubbles. We conducted mechanistic studies of sonoporation with cells cultured on the hydrogel with elasticity modulus of 0.2 kPa and 40 kPa, mimicking soft and stiff tissue microenvironments, respectively. RGD-linked targeted microbubbles, binding to the integrins, were employed to exert well-controlled, localized subcellular actuation on the cell membrane. We first studied the initial attachment between targeted microbubbles and the cell membrane using a unique imaging strategy that we developed. Then we investigated the acoustic activities of microbubbles upon ultrasound excitation recorded by high-speed video microscopy. Finally, we explored the cell membrane permeabilization achieved by targeted microbubbles and ultrasound. Our results demonstrate that ECM rigidity profoundly affects sonoporation facilitated by targeted microbubbles.

2. Materials and methods

2.1. Hydrogel fabrication

Extracellular matrix substrates consisting of polyacrylamide hydrogels with different rigidity were produced by adjusting the concentration of the monomer, acrylamide and the crosslinker, bis-acrylamide (Sigma-Aldrich, St. Louis, MO, USA) [32]. All the hydrogels were fabricated on centers of glass bottom dishes with a height of about 70 μm. The stiffness of the gels was measured with an Atomic Force Microscope (AFM, Bruker, Germany). Hydrogels with elastic modulus of 0.2 kPa and 40 kPa were applied to mimic the soft and stiff tissues for sonoporation experiment.

2.2. Cell culture on gels

The hydrogel surface was activated by a cross-linker sulfo-SANPAH (Sigma-Aldrich, St. Louis, MO, USA), which induced catalysis action when exposed to 365-nm UV light for 30 min. Collagen I (Invitrogen, Carlsbad, CA, USA, USA) was diluted in PBS to a concentration of 50 μg/ml and was absorbed to gel surface for cell culture. NIH 3 T3 cells (ATCC, Gaithersburg, Maryland, USA) were used to investigate the details of sonoporation affected by ECM rigidity. One day before the experiment, cells were adhered to the hydrogels to reach 60% confluency in Dulbecco's Modified Eagle Medium (Gibco, Merelbeke, Belgium) supplemented with 10% (v/v) fetal bovine serum (FBS, Biolnd, Isreal), 100 U/mL penicillin and 100 μg/mL streptomycin in a humidified incubator at 37 °C with 5% CO_2.

2.3. Ultrasound apparatus and microbubbles

A non-focused ultrasound transducer (1.5 MHz, Jiangyin AD Ultrasonic Technology Inc, China) was applied to trigger sonoporation. It was positioned at a 45° angle, about 8.5 mm (Rayleigh distance) from the cells (Fig. 1A), with its active surface submerged in PBS. A single-pulse sinusoidal signal from a waveform function generator (33250A, Agilent Technologies, Santa Clara, CA, USA) was amplified by a 100 W power amplifier (75A250A, Amplifier Research, USA). An inverted fluorescence microscope (Axio Observer A1, Carl Zeiss, Germany) was applied to capture details of sonoporation. A 40 μm calibration needle hydrophone (Precision Acoustics HPM04/1, UK) was applied to pre-characterize the transducer in the free filed.

SIMB4-5 (Advanced Microbubbles laboratories LLC, Boulder, CO, USA) targeted microbubbles decorated with streptavidin were used. Biotin-RGD peptides (PCI-3697-PI, Peptides, Louisville, KY, USA) were conjugated onto microbubble shells to generate RGD-modified microbubbles. A Zetasizer nano ZS90 (Malvern, England) was applied to measure physiochemical properties of microbubbles and RGD-modified microbubbles. As shown in Table 1, RGD modification didn't significantly change the diameter, zeta potential and polydispersity index (PDI) of the microbubbles.

Next, a 10 μL solution of microbubbles (1×10^9 bubble/mL) was incubated with a solution of 1.5 μL Biotin-RGD peptides (1 mg/mL) for 20 min at room temperature. After removing the culture medium, 10 μL of the RGD-decorated bubble solution was added immediately on the hydrogels with cells instantly. The dish was then flipped upside down for 10 min to allow the bubbles to conjugate with cells. The unbound microbubbles were gently washed away using PBS before the experiments. Illustrations and bright field microscopic images of cells on soft

Table 1
The physiochemical properties of microbubbles and RGD-modified microbubbles.

Bubble type	Parameters		
	Mean diameter (μm)	Zeta potential (mV)	PDI
Microbubbles	3.42 ± 0.39	− 5.73 ± 3.03	0.0785 ± 0.0446
RGD-modified Microbubbles	3.07 ± 0.07	− 6.72 ± 2.76	0.0742 ± 0.0187

and rigid substrates with a targeted microbubble attached are shown in Fig. 1.

2.4. Resolving detailed attachment configurations

NIH 3T3 cells were cultured on 0.2 kPa and 40 kPa gels 24 h before imaging. Calcein blue (50 μg/ml, M1255, Sigma-Aldrich, St. Louis, MO, USA), an impermeable fluorescent reagent, was dissolved in the medium. It is excluded from the cell and bubbles (Fig. 2A), thereby indicating the boundaries of the cell with bubbles as a whole structure. Calcein-AM (C3099, Invitrogen, Carlsbad, CA, USA), was used to indicate the boundaries of (live) cells (Fig. 2B). A 100× silicone oil immersion objective, equipped on a confocal fluorescence microscope (Nikon A1, Melville, NY, USA) was used to capture detailed spatial relationship between targeted microbubbles and cell membrane in 3D. The scanning step was set to 125 nm in z direction (Fig. 2C).

Huygens software was applied to estimate the point spread function (PSF) of the light source in the confocal microscope. The bubble-cell fluorescence images were first deconvoluted with the PSF to correct the optical distortion associated with the light source. Based on the Mumford-Shah function for segmentation, the Chan-Vese algorithm [33] was employed to detect the microbubble-cell boundaries using a customized MATLAB code (Fig. 2). The number of slices showing the connection between microbubbles and cell membrane were in the range of five to fifteen. The microbubble-cell contact length, the height and the arc length of cell membrane stretched by microbubbles were measured in Image J using the superimposed boundary detection results from two independent fluorescence channels.

2.5. High-speed video-microscopy of ultrasound-excited bubble activities and data processing

A high-speed camera (Photron FASTCAM SA-X2, San Diego, CA, USA) was employed to capture microbubble dynamics activated by ultrasound. The recording frame rate was 100 K frames/s, while the field of view was set to be 256 × 256 pixels. Brightfield movies from before ultrasound to 200 ms post ultrasound were recorded. Still images
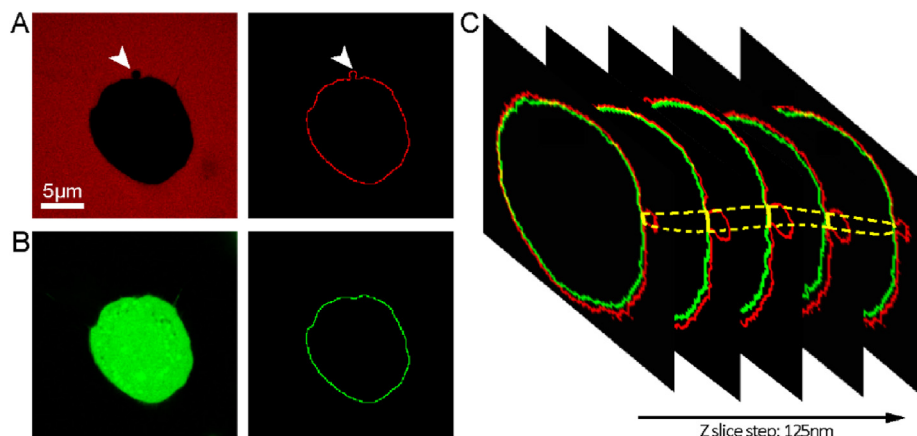
were also captured 300 s post ultrasound.

Bubble size and position was extracted using a customized MATLAB code. Microbubble deformation index was defined as the ratio between the maximum and the minimum radii of curvature of a bubble. Microbubble displacement was defined as the translational movement distance of the center of the bubble relative to that before ultrasound. To quantify the post ultrasound bubble radius change dynamics, Epstein-Plesset (EP) equation was used to fit the microbubble dissolution process [34]. This model assumes a perfectly spherical geometry throughout dissolution and neglects changes in the shell properties as it deforms to accommodate the shrinking gas core:

$$- \frac{dr}{dt} = \frac{L}{\frac{r}{D_w} + R_{shell}} \left(\frac{1 + \frac{2\sigma_{shell}}{P_a r} - f}{1 + \frac{3\sigma_{shell}}{4P_a r}} \right), \tag{1}$$

where r(t) is the microbubble radius, L is Ostwald's coefficient, D_w is the gas diffusivity in water, R_{shell} is the resistance of the shell to gas permeation, σ_{shell} is the surface tension of the shell, and f is the ratio of the gas concentration in the bulk medium versus that at saturation.

2.6. Tracking the dynamics of cell membrane permeabilization

Single pulse ultrasound (0.45 MPa, 10 μs) was applied to excite microbubbles. Propidium iodide (PI, 668 Da, 100 μM, Sigma-Aldrich, St. Louis, MO, USA), a cell-impermeable small molecule, was used to indicate pore formation and resealing process. A cooled CCD camera (PCO. 1600, Kelheim, Germany) was applied to record real-time PI fluorescence images. Calcein-AM (Invitrogen, Carlsbad, CA, USA, USA) was added 300 s post ultrasound to assay cell viability. The concentration gradient driven influx of PI molecule through the pore can be modeled as a steady-state diffusion process, which is governed by the Fick's first law. And the pore resealing process can be treated as a single exponential function. The total PI-nucleic acid complex intensity inside a cell, which is proportional to the PI molecule number, can be described by the following equation:

$$F(t) = \alpha \cdot \pi D C_0 r_0 \cdot \frac{1}{\beta} (1 - e^{-\beta t}), \tag{2}$$

where α is the coefficient between PI-nucleic acid complex fluorescence intensity and the number of PI molecule, D is the diffusion coefficient of PI molecule (200 μm²/s [35]), C_0 is the extracellular concentration of PI, r_0 is the initial radius of pore created on the cell membrane, and β is the pore resealing time constant, which is estimated by fitting the PI intensity-time curve. The coefficient α was measured from a series of PI-RNA solutions with different known concentration in customized polydimethylsiloxane (PDMS, Dow Corning sylgard 184, Midland, MI, USA) micro-channels, as the method developed in our previous study [30]. Fluorescence intensity of the PI-DNA complex is 2.3 times of PI-

Fig. 2. (A) A fluorescence image in blue channel (for display purpose, pseudo-colored to be red) and the detected boundary of the cell with an attached microbubble (arrows point) as a whole structure. (B) A fluorescence image in green channel and the detected boundary of the cell. (C) Boundary detection results from a series of images. (For interpretation of the references to colour in this figure legend, the reader is referred to the web version of this article.)

Z slice step: 125nm

RNA [36] at the same concentration. This factor was used to correct the fluorescent intensity in nucleus.

2.7. Cell staining and confocal fluorescence microscopy

After cells on 0.2 kPa and 40 kPa gels were conjugated with microbubbles, they were fixed with 4% paraformaldehyde (Solarbio, China) for 10 min at room temperature. After washing with PBS twice, the cells were permeabilized in 0.2% Triton-X (Merck KGaA, Darmstadt, Germany) for 10 min, and blocked in 5% BSA (Invitrogen, USA) for 1 h. Primary antibody (Rabbit Anti-Integrin Alpha V & Beta 3 antibody, 1:200, Alpha Lifetech, San Francisco, CA, USA) targeting αvβ3 integrins was incubated for 1 h at room temperature with gentle shaking on a microplate shaker (Thermo Fishier, Wilmington, DE, USA). The hydrogels were washed twice in PBS and incubated in secondary antibody (Alexa Fluor 594 Donkey Anti-Rabbit IgG (H + L) Antibody, 1:200, Invitrogen, Carlsbad, CA, USA) for 1 h at room temperature. A confocal fluorescence microscope (Olympus, Melville, NY, Japan) with a PLAN APO N 60X Oil objective was applied to image the distribution of integrins (561 nm stimulation) on the cell surface. The scanning step was set to 1 μm in z direction.

2.8. Statistics analysis

All experiments were repeated at least three times independently. To test significance, the experimental data was analyzed using the Mann-Whitney U test (between two groups without assumption of normal distribution). All the statistical analysis was carried out in SPSS 25 Statistics V.25.0 software (IBM Corp., Armonk, NY, USA).

3. Results

3.1. Characterization of bindings between targeted microbubbles and integrins

To study the impact of ECM rigidity on sonoporation, we cultured fibroblast NIH 3T3 cells, a known mechanically sensitive cell line, on 0.2 kPa and 40 kPa gel substrates mimicking soft and rigid tissue microenvironments (Fig. 1B–E). On the soft substrate, the cells had rounded morphology, while on the rigid substrate, cells were well spread. For cells on the rigid substrate, 21.6% (94 out of 436) cells had more than three bubbles attached, while only 2.2% (5 out of 228) cells on the soft substrate had more than three bubbles attached (Fig. 1F). The immunofluorescence images of αvβ3 integrins show that αvβ3 integrins were aggregated at RGD-microbubble-attached positions on the cell surface. For cells cultured on the rigid substrate, the integrin clusters were larger and with stronger fluorescence intensity (Fig. 3).

3.2. Initial attachment configurations of targeted microbubbles

We developed a unique strategy to resolve the detailed 3D spatial relationship between targeted microbubbles and cell membrane. Independent and complementary information was obtained from two fluorescence channels, blue and green (Fig. 2). The results showed that the majority of the bubbles clearly contacted with the cell membrane both for cells on soft (73.8%, 31 bubbles out of 42) and rigid (70.6%, 12 bubbles out of 17) substrates. Specifically, there were two types of attachment configurations included, type A and type B. In type A attachment, a small portion of the bubble shell was attached on the cell membrane without causing any deformation of the membrane (Fig. 4A–C). Microbubbles attached to the cells on the soft substrate presented smaller contact length (23.4 ± 6.8%, N = 4, n = 19 bubbles) compared with cells on the rigid substrate (29.1 ± 4.5%, N = 3, n = 7 bubbles) (Fig. 4D). In type B attachment, the microbubble-attached local membrane was stretched, which was due to the buoyancy of the microbubble. The height of the raised local membrane was

0.50 ± 0.09 μm for cells on the soft substrate (N = 4, n = 12 bubbles), and 0.85 ± 0.12 μm for cells on the rigid substrate (N = 3, n = 5 bubbles) (Fig. 4 H), suggesting that the microbubbles attached to the cells on rigid substrate had stronger ability to pull on the membrane.

In addition, we observed another four types of attachment configurations, type C–F (Fig. 5), with a much lower frequency of occurrence (Table 2). The common feature of types C and D attachment was the "gap" (in a range of 0.49 μm–1.43 μm) between the bubbles and the cell membrane. We speculated that the connection between bubbles and cell membrane was via very thin tethers. As suggested by previous experiments with optical tweezers [37] and an AFM [38], the tether radius might be around 50–100 nm, which is under the resolution of the light microscope. Therefore, we were unable to visualize it. The distinctive feature of type D was the raised local membrane underneath the "gap", which was undoubted evidence showing that the bubble had exerted force on the local membrane through the thin tether. In contrast, in types E and F attachment, some portion or all of the bubble surface was surrounded by the cell membrane or cytoplasm. In type E, the bubble-attached cell membrane was sunken, while in type F, the bubble was completely engulfed inside the cell. Type E and F were only observed in cells on the soft substrate, not in cells on the rigid substrate.

3.3. Acoustic activities of targeted microbubbles

High-speed video microscopy recording at a speed of 100 K frames per second (8.9 μs exposure time per frame) was employed to capture the details of the bubble-cell interaction during and post ultrasound application (a single pulse with acoustic pressure 0.45 MPa and duration 10 μs) (Fig. 6A and B). Bubble expansion was shown clearly in the ultrasound-on frame (at 10 μs), reflecting its volumetric oscillation during ultrasound stimulation. All data with ΔR > 0.5 μm showed that bubbles attached to cells on the rigid substrate exhibited larger expansion and therefore stronger shear stress onto the cell membrane (Fig. 6C and D), which was estimated using Newton's law of viscosity assuming a "no-slip" boundary condition [39]. This observation indicated that bubbles attached to cells on the rigid substrate underwent more violent oscillation, which was supported by the residual bubble size at 5 min post ultrasound.

At 5 min post ultrasound, the residual bubble radius for cells on the rigid substrate (1.39 ± 0.38 μm, n = 81) was significantly smaller than that for cells on the soft substrate (1.83 ± 0.44 μm, n = 58), even with the similar initial bubble radius (Fig. 7A and B), reflecting more gas lost induced by ultrasound stimulation. The fact that most bubbles still existed 5 min post ultrasound (58 out of 62 for bubbles attached to cells on the soft substrate, and 81 out of 87 for bubbles attached to cells on the rigid substrate) indicated that the lipid shell persisted during ultrasound exposure. We fitted the bubble radius-time curve over the first 200 ms post ultrasound using dissolution models. For all the bubbles that remained at 5 min post ultrasound, the curves were best fit with a dissolution model with a shell, while for all the bubbles that disappeared at 5 min post ultrasound, the curves were best fit with a dissolution model without a shell. The fitting revealed a mixture of perfluorocarbon (in the range of 8%–87%) and air (in the range of 3%–92%) in the gas core. The composition of each bubble was highly heterogenous and was independent of ECM rigidity.

More interesting phenomena were observed shortly (at 30 μs) after ultrasound was turned off. Among all the bubbles attached to the cells on the soft substrate, 32.3% (20 out of 62) exhibited strong deformation (deformation index in the range of 2.51–5.53, where deformation index was defined as the ratio between the maximum and the minimum radii of curvature of a bubble.), coupled with the large displacement (Fig. 8A, C and D), suggesting that bubble-cell interaction lasted at least 20 μs post ultrasound for cells on the soft substrate. The bubbles attached to the cells on the rigid substrate showed little deformation overall (Fig. 8B–F).
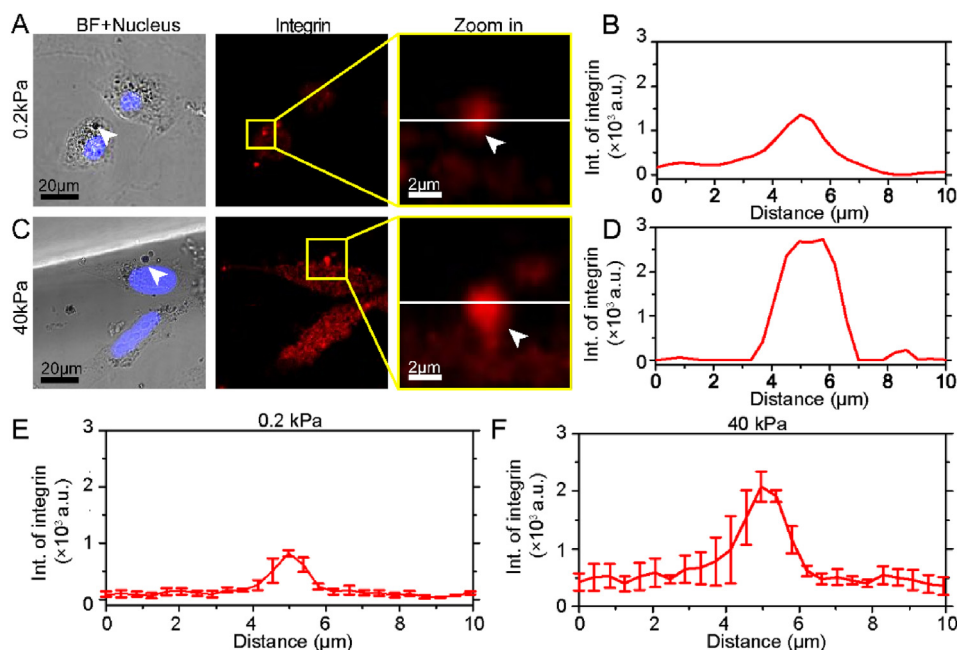
Fig. 3. Integrin expression and distribution of cells cultured on soft and rigid substrates. Bright field images and immunofluorescence images of integrins (A, C) and the fluorescence intensity line profiles (B, D) of the lines drawn in the zoom-in images of cells on soft and rigid substrates respectively. Averaged fluorescence intensity line profiles of integrins of cells on soft (E) and rigid (F) substrates. Each substrate, N = 3, n = 5. (B–F) all centered at the microbubble. Error bar, s.e.m.

3.4. Cell membrane permeabilization

Cell membrane-impermeable small molecule propidium iodide (PI) was used to indicate the cell membrane permeabilization. For cells cultured on both soft and rigid substrates, the cell viability decreased with the increase of acoustic pressure (Fig. 9A). For cells on the soft substrate, sonoporation occurred when acoustic pressure reached 0.45 MPa, while for cells on the rigid substrate, that number was 0.3 MPa (Fig. 9B), indicating that higher acoustic pressure was needed to permeabilize the cell membrane for cells cultured on the soft substrate.

When exposed to the ultrasound pulse (0.45 MPa, 10 μs), the microbubbles induced pore formation on the local membrane, allowing the influx of the PI molecule and forming red fluorescence complexes with nucleic acid inside the cell (Fig. 10A and B). A calcein AM assay 5 min post ultrasound (Fig. 10A and B) indicated that the pore was successfully resealed. The time course of the fluorescence intensity of the total PI-nucleic acid complex, after the fluorescence intensity inside the nucleus was corrected, is plotted in Fig. 10C. The cells on the rigid substrate obtained more PI molecule than cells on the soft substrate at 5 min post ultrasound (Fig. 10D) ($0.67 \pm 0.04 \times 10^5$ a.u., N = 5, n = 36 cells on 0.2 kPa gel; $0.87 \pm 0.06 \times 10^5$ a.u., N = 3, n = 38
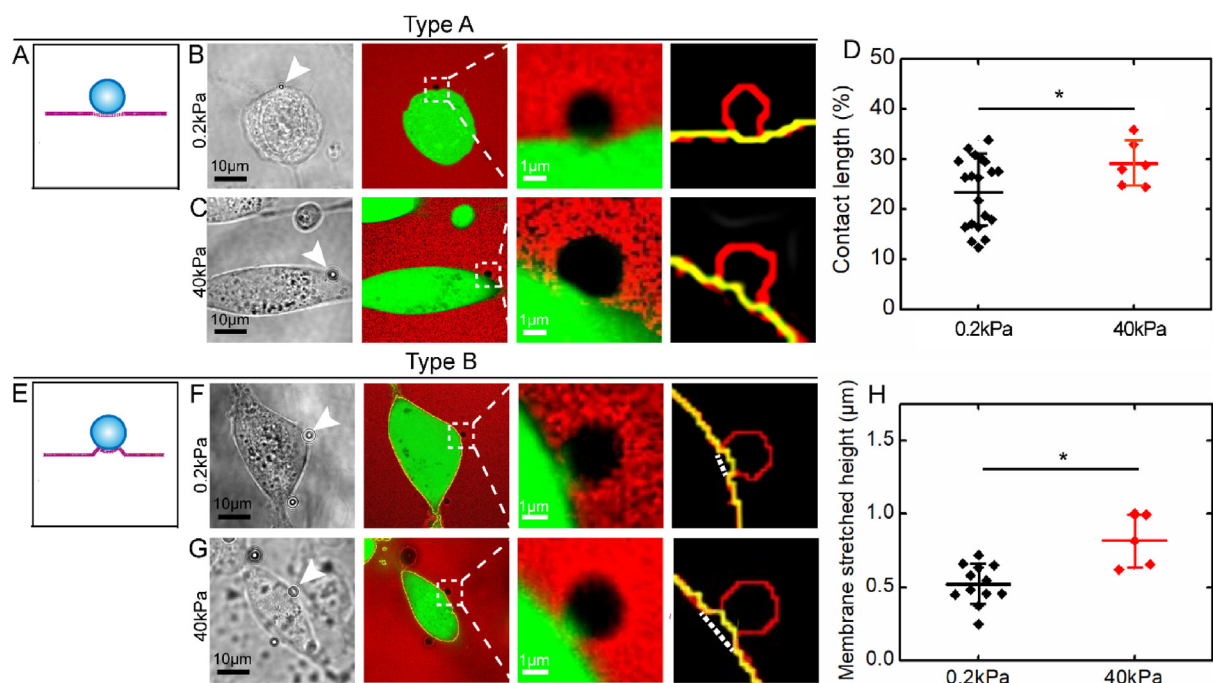

Fig. 4. Targeted microbubble attachment configurations with contact to the cell membrane, type A (A–D) and type B (E–H). Schematic illustrations (A, E), representative bright field images, fluorescence images superimposed from two channels and the corresponding boundary detection results (B, C, F, G) for each type. (D) The relative maximum contact length, calculated as the maximum contact length divided by the bubble perimeter, for cells in type A. (H) Cell membrane stretched height by targeted microbubbles for cells in type B. Significance was tested using Mann Whitney *U* test. *, p < 0.05. Error bars, s.d.
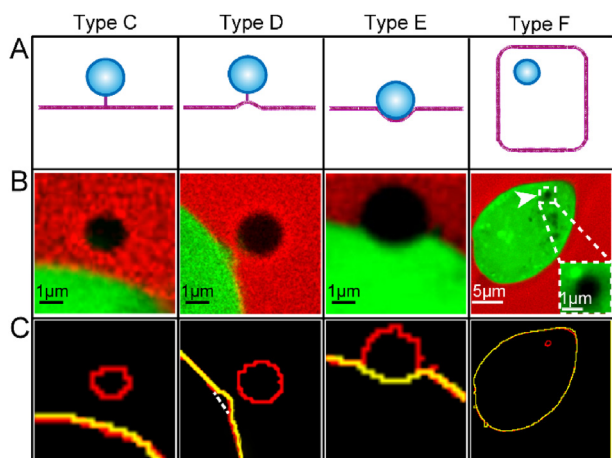
Fig. 5. Targeted microbubble attachment configurations, type C–F. Schematic illustrations (A), representative fluorescence images superimposed from two channels (B), and the corresponding boundary detection results (C) for each type.

Table 2

Occurrence of different microbubble attachment types.

Occurrence	Attach type					
	A	B	C	D	E	F
0.2 kPa (Total: 42)	19	12	5	1	2	3
40 kPa (Total: 17)	7	5	5	0	0	0

size and the time constants of the resealing process. The results showed that for the same ultrasound stimulation (0.45 MPa, 10 μs), a smaller pore was generated for cells on the rigid substrate (Fig. 10E) (19.4 ± 6.9 nm, N = 5, n = 36 cells on 0.2 kPa gel; 12.1 ± 6.7 nm, N = 3, n = 38 cells on 40 kPa gel), but with slower resealing process (Fig. 10F) (resealing time constant $8.98 \pm 0.43 \times 10^{-2}$ s^{-1}, $R^2 = 0.95 \pm 0.06$, N = 5, n = 36 cells on 0.2 kPa gel; $4.35 \pm 0.27 \times 10^{-2}$ s^{-1}, $R^2 = 0.94 \pm 0.05$, N = 3, n = 38 cells on 40 kPa gel). The slower resealing process could benefit the cells on the rigid substrate for more exogenous therapeutic agent uptake. Meanwhile, it could also expose the cells to a higher risk of unsuccessful recovery, which might be responsible for the lower survivability with PI uptake for cells on the rigid substrate (Fig. 9).

4. Discussion

In this study, we investigated the impact of ECM rigidity onto sonoporation facilitated by targeted microbubbles by integrating physiologically relevant ECM rigidity into a mechanistic study of sonoporation at the single-cell level. We found that the multiple aspects of the process, from the initial microbubble attachment, to ultrasound-driven microbubble activities, to the final cell membrane permeabilization, were all dependent on ECM rigidity.

The employment of targeted microbubbles enables the selective accumulation of microbubbles onto the targeted cells, therefore effectively increasing the targeted cells vulnerability upon ultrasound stimulation and reducing undesired side effects. As the initial condition of microbubble acoustic activity, the attachment configuration deeply influences the bubble-cell interaction and consequential downstream bioeffects. The conventional approach to study the microbubble structure was to fluorescently label the bubble shell [40–42]. However, problems, such as weakness of the fluorescence signals, uneven labeling, undesired labeling of cell membrane, might be associated with this approach. Moreover, super-resolution microscopy is often needed to resolve the nanometer scale of the shell thickness, which might
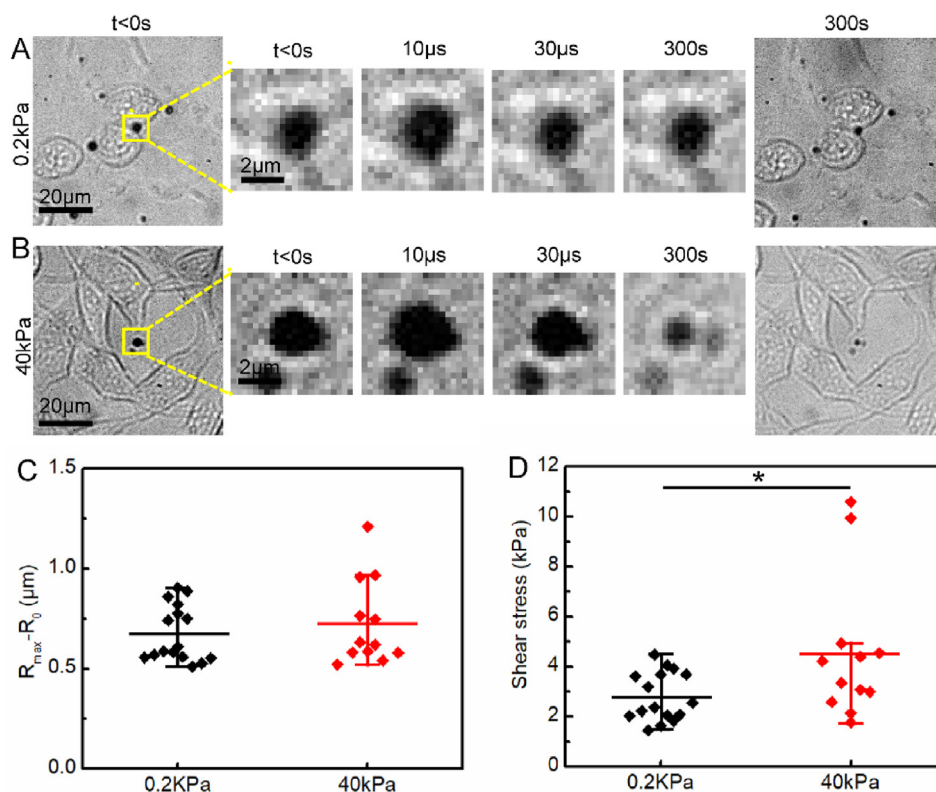
cells on 40 kPa gel).

A quasi-steady 2D diffusion model of the PI molecule combined with an exponential model of the pore resealing process [30] was used to fit the PI fluorescence intensity-time curve so as to estimate the initial pore

Fig. 6. Acoustic activities of microbubbles driven by ultrasound. Selected image sequences of microbubbles excited by ultrasound (0.45 MPa, 10 μs) attached to cells on soft (A) and rigid (B) substrates. (C) Microbubble expansion (ΔR > 0.5 μm) in the ultrasound-on frame. (D) The corresponding maximum shear stress derived from microbubble expansion. Significance was tested using Mann Whitney *U* test. *, p < 0.05. Error bars, s.d.
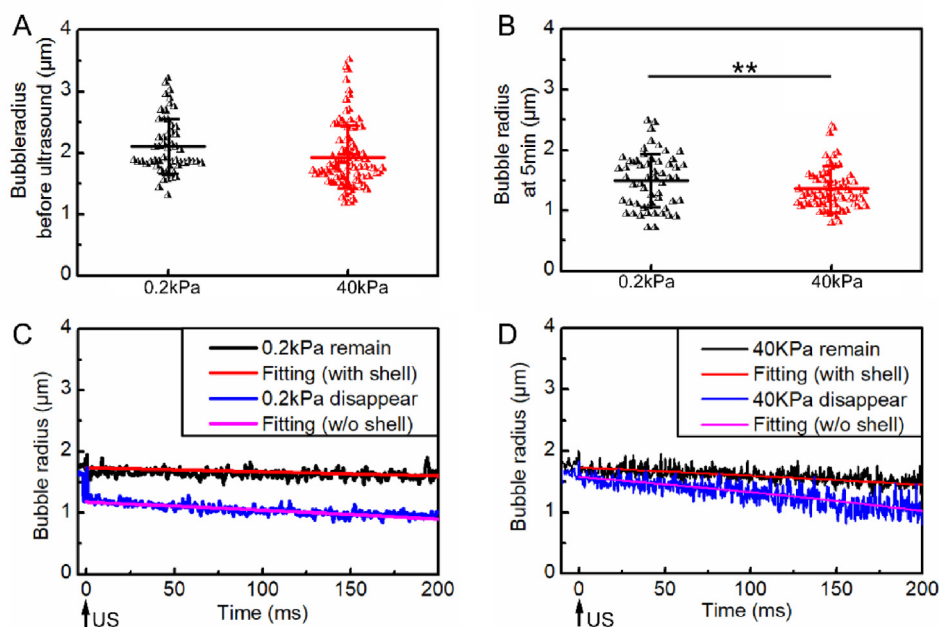
Fig. 7. Microbubble radius before ultrasound stimulation (A) and 5 min post ultrasound (B). Representative bubble radius changes over 200 ms post ultrasound, fitted with a dissolution model with or without lipid shell for cells on soft (C) and rigid (D) substrates. Significance was tested using Mann Whitney *U* test. *, $p < 0.05$; **, $p < 0.01$. Error bars, s.d.

further limit the application of this approach.

In this study, we developed a simple but effective imaging strategy to visualize the details of the attachment configurations between targeted microbubbles and cell membrane in 3D. The strong and clear contrast between black (the cell with bubbles) and blue (outside the cell and bubbles) in blue fluorescence channel, and black (outside the cell) and green (inside the cell) in green fluorescence channel (Fig. 2), provided high-quality fluorescence images and ensured the high accuracy of boundary detection in post image processing. Without delicate labeling procedures nor the involvement of super-resolution microscopy, this robust and user-friendly method can be readily extended to visualize details of other micron-scale subjects.

As compared to a previous study, where hydrogel-coated quartz glasses linked with streptavidin was used [43], we elucidated the 3D attachment configurations between targeted microbubbles and cells via RGD-integrin linkage, a setting more relevant to in vivo. Because of the fluidity and elasticity of the cell membrane, we observed several types of cell membrane deformation induced by targeted microbubble attachment, including the local membrane stretched (type B, Fig. 4), the local membrane stretched through a thin tether (type D, Fig. 5) and the local membrane sunken (type E, Fig. 5). All these interesting new findings can only be obtained when a cell, rather than a substrate, was employed.

Compared with sonoporation facilitated by free bubbles, sonoporation facilitated by targeted microbubbles is subjected to stronger effects imposed by ECM rigidity, as the expression of receptors and cell functions are often regulated by ECM rigidity. In this study, we used RGD-linked microbubbles, which binds with integrins and thereafter, were held on the cell membrane. It is reported by previous studies that the overall integrin expression for cells on the rigid substrate is higher than that on the soft substrate [44,45]. In this study, we provide more details about the interaction between RGD-microbubbles and integrins on soft and rigid ECM. We found that more bubbles were attached to cells on the rigid substrate (Fig. 1F), larger integrin clusters with stronger fluorescence intensity appeared at microbubble attachment sites for cells on the rigid substrate (Fig. 3), and tighter connections between bubbles and cell membrane were formed for the cells on the rigid substrate (Fig. 4).

Some cell functions regulated by ECM rigidity may directly explain some observations obtained in this study. For example, in the initial bubble attachment configurations, type E (cell membrane sunken at

microbubble attached position) and type F (the microbubble was engulfed inside the cell) attachments were only observed for cells on the soft substrate, not on the rigid substrate. This observation may be attributed to promoted endocytosis by soft substrates [45–47]. As shown in Fig. 8, at 5 min post ultrasound, bubbles attached to cells on the rigid substrate exhibited larger displacement than bubbles attached to cells on the soft substrate. Since 5 min are far beyond the timescale of the ultrasound pulse, this observation may be ascribed to the enhanced cell motility regulated by rigid substrates [48].

We employed a 100 K frames/s high-speed camera to capture bubble dynamics driven by ultrasound up to 200 ms. The 8.9 µs exposure time allowed us to capture bubble expansion during ultrasound exposure (0.45 MPa, 10 µs), and 200 ms recordings were able to cover the bubble dissolution dynamics post ultrasound. Based on bubble expansion, we further calculated the shear stress and found out that for all data with $\Delta R > 0.5$ µm, bubbles attached to cells on the rigid substrate exhibited larger expansion and stronger shear stress. For all data with $\Delta R \leq 0.5$ µm, no significant difference was detected between bubbles attached to cells on soft and rigid substrates, which may be limited by the sensitivity of our imaging system. We are fully aware that the bubble expansion detected using our high-speed camera was very likely to be underestimated due to the relatively long exposure time. Even so, our results were comparable with the results obtained by an ultrafast camera [29].

The most interesting phenomenon observed was that one-third of the bubbles attached to the cells on the soft substrate presented strong deformation shortly (at 30 µs) after ultrasound was turned off (Fig. 8). The asymmetric oscillation of ultrasound excited targeted microbubbles adherent to a surface was observed by ultrafast microscopic imaging and described mathematically [1]. Contacting with a wall resulted into an asymmetric oscillation of non-targeted bubbles exposed to ultrasound [49,50]. Microstreaming and other factors may be responsible for the continued bubble-cell interaction shortly post ultrasound. The microstreaming generated around oscillating bubbles [5,51] lasted tens of microseconds post ultrasound [1]. An oscillating bubble can induce fluctuation in its nearby elastic surfaces, and softer materials will have the larger amplitude fluctuations [52]. The sustained fluctuation of the cell membrane could be another driving force for the bubble-cell interaction post ultrasound.

Although in most studies reported so far, the shell of microbubbles is composed of a protein or lipid or polymer, recent advances are being
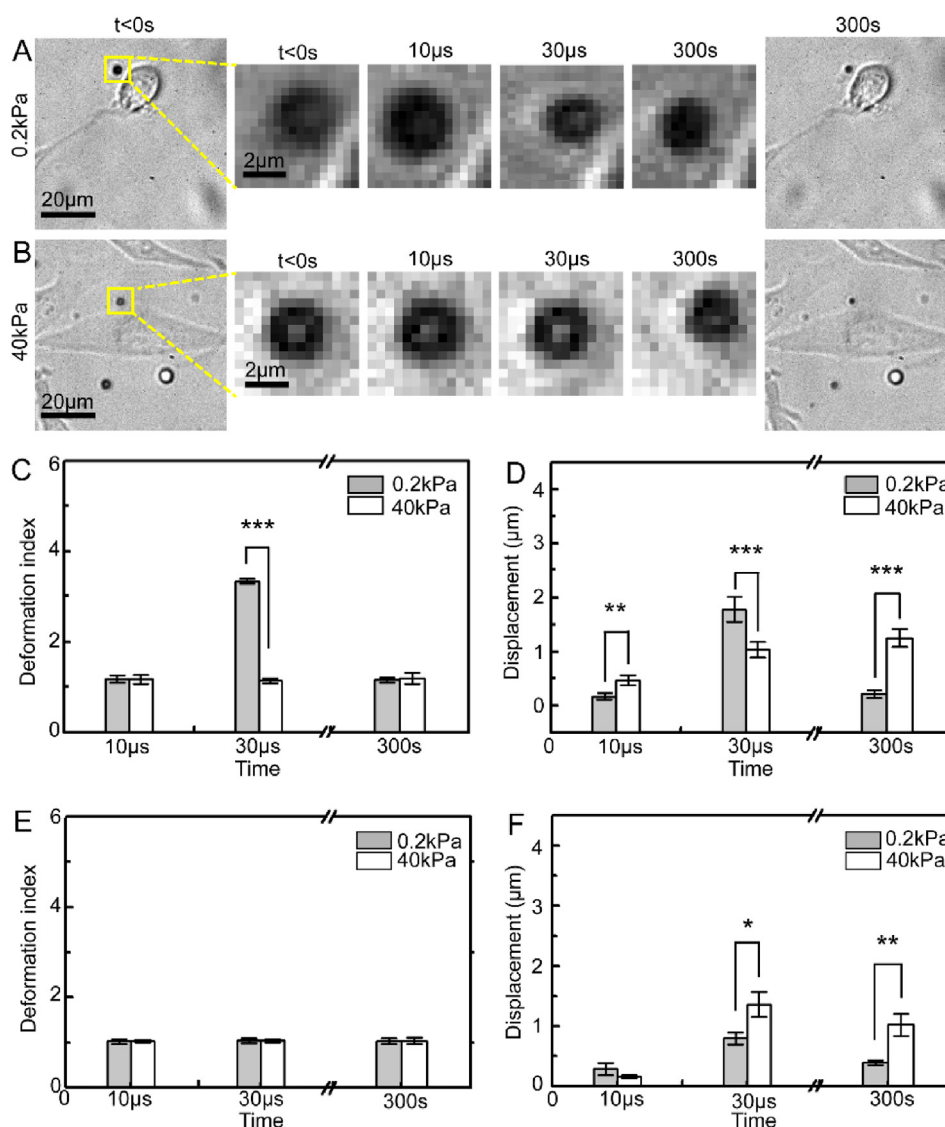
Fig. 8. Selected image sequences of microbubbles excited by ultrasound (0.45 MPa, 10 μs) attached to cells on soft (A) and rigid (B) substrates. Microbubble deformation and displacement, for bubbles with deformation index > 1.05 (C, D) and bubbles with deformation index < 1.05 (E, F) at 10 μs, 30 μs and 300 s. Significance was tested using Mann Whitney U test. *, $p < 0.05$; **, $p < 0.01$; ***, $p < 0.001$. Error bars, s.e.m.

made to explore the new possibility for the microbubble shell materials. A recent theoretical study found that a liquid-crystalline shelled microbubble could significantly enhance the wall shear stress on a rigid plane [53]. Lysozyme-shelled microbubbles were reported to offer advantages over conventional microbubbles for tuning their functional

properties [54]. A cloaked-surface architecture has been employed to design microbubbles to minimize unwanted interactions and immunogenicity for ultrasound molecular imaging [55].

Sonoporation facilitated by targeted microbubbles consists of a series of key events, where microbubble acoustic activities play the
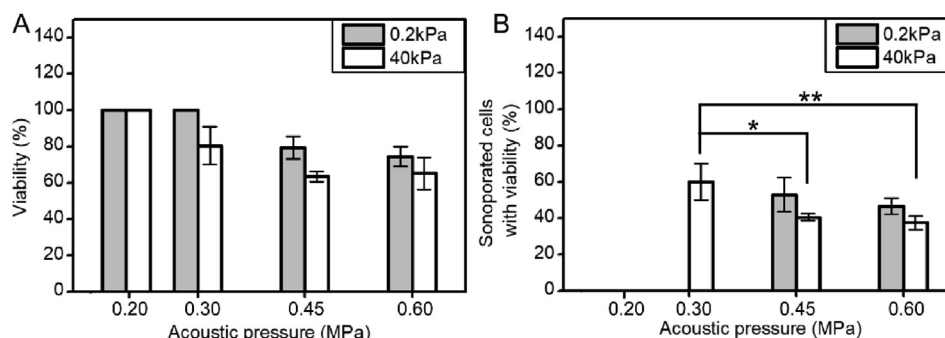

Fig. 9. Cell viability (A) and PI delivery efficiency (B) for cells cultured on soft and rigid substrates. Significance was tested using ANOVA test. *, $p < 0.05$; **, $p < 0.01$. Error bars, s.d.
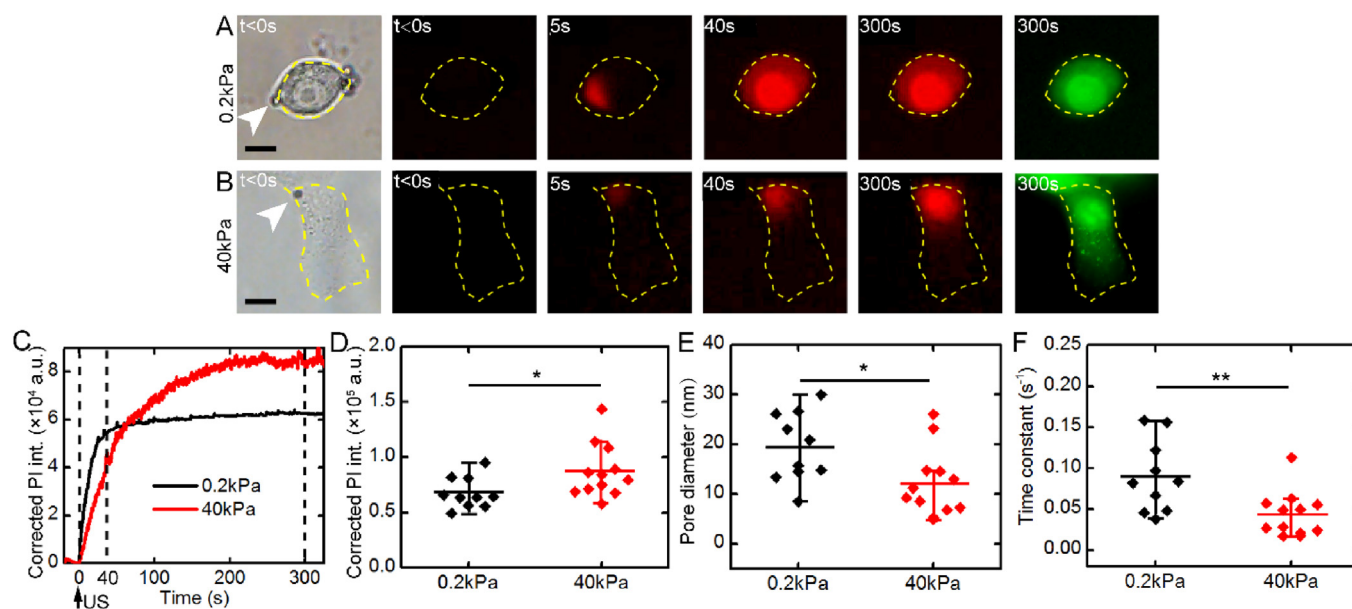
Fig. 10. Selected image sequences show the dynamic process of PI influx into the cell from targeted-microbubble-attached locations (arrows point) and diffusion inside the cell for cells on (A) soft and (B) rigid substrates. A post ultrasound (at 300 s) calcein-AM assay showed the retention of calcein inside the cells. (C) Corrected total intracellular PI-nucleic acid complex fluorescence intensity change over time for data shown in (A) and (B). (D) Total intracellular PI intensity measured at 300 s post ultrasound. (E) Pore diameter. (F) Pore closure time constant. Significance was tested using Mann Whitney U test. *, $p < 0.05$; **, $p < 0.01$. Error bars, s.d.

pivotal role. At the microbubble attached site, the initial bubble attachment configuration, combined with the local cell membrane elasticity, led to certain bubble acoustic activities upon ultrasound excitation, and consequently the pore formation. Afterwards, the pore resealing process determined the pore opening period and, therein, the total exogenous therapeutic agent uptake and cell survivability. By regulating the expression of cell surface receptors, cellular mechanical properties (e.g., cell morphology and cell stiffness), and related cell functions (e.g., endocytosis and cytoskeleton rearrangement, associated with pore resealing), ECM rigidity serves as an active player in sonoporation facilitated by targeted microbubbles. Taken all together, the current results suggest that for cells on the soft substrate, the relatively loose initial attachment of targeted microbubbles and the gentle but longer bubble-cell interaction generated larger pores on the cell membrane, without severely compromising cell viability. In contrast, for cells on the rigid substrate, the tight initial attachment of targeted microbubbles and the more violent bubble-cell interaction driven by ultrasound generated smaller pores on the cell membrane.

5. Conclusion

This study revealed the impact of ECM rigidity on sonoporation facilitated by targeted microbubbles, by conducting a mechanistic study of single cells cultured on soft and rigid substrates. The resolved 3D attachment configurations imply that targeted microbubbles formed stronger connections to the cell membrane via RGD-integrin bindings for cells on the rigid substrate. The high-speed video microscopy of bubble dynamics excited by ultrasound suggest that more violent acoustic activities occur for bubbles attached to cells on the rigid substrate. The experiments of cell membrane permeabilization stimulated upon a short ultrasound pulse indicate that smaller pores accompanied with a slower resealing process were generated on cells cultured on the rigid substrate. Our results demonstrate that the ECM rigidity profoundly affects the bubble-cell interaction and therefore the cell membrane permeabilization. The current findings may benefit the rational development of sonoporation technique and its ongoing clinical translation.

CRediT authorship contribution statement

Ning Rong: Conceptualization, Methodology, Software, Formal analysis, Investigation, Writing - original draft. **Meiru Zhang:** Methodology, Software, Investigation, Writing - original draft. **Yulin Wang:** Methodology, Investigation. **Hao Wu:** Software, Formal analysis. **Hui Qi:** Methodology. **Xing Fu:** Resources. **Dachao Li:** Resources. **Chunmei Yang:** Formal analysis. **Yan Wang:** Resources. **Zhenzhen Fan:** Conceptualization, Methodology, Writing - original draft, Supervision.

Declaration of Competing Interest

The authors declare that they have no known competing financial interests or personal relationships that could have appeared to influence the work reported in this paper.

Acknowledgments

References

[1] G. Lajoinie, Y. Luan, E. Gelderblom, B. Dollet, F. Mastik, H. Dewitte, I. Lentacker, N. de Jong, M. Versluis, Non-spherical oscillations drive the ultrasound-mediated release from targeted microbubbles, Commun. Phys. 1 (2018).

[2] Z. Fan, D. Chen, C.X. Deng, Characterization of the dynamic activities of a population of microbubbles driven by pulsed ultrasound exposure in sonoporation, Ultrasound Med. Biol. 40 (2014) 1260–1272.

[3] A. van Wamel, K. Kooiman, M. Harteveld, M. Emmer, F.J. ten Cate, M. Versluis, N. de Jong, Vibrating microbubbles poking individual cells: drug transfer into cells via sonoporation, J. Control. Release 112 (2006) 149–155.

[4] P. Prentice, A. Cuschierp, K. Dholakia, M. Prausnitz, P. Campbell, Membrane disruption by optically controlled microbubble cavitation, Nat. Phys. 1 (2005) 107–110.

[5] P. Marmottant, S. Hilgenfeldt, Controlled vesicle deformation and lysis by single oscillating bubbles, Nature 423 (2003) 153–156.

[6] G. Dimcevski, S. Kotopoulis, T. Bjanes, D. Hoem, J. Schjott, B.T. Gjertsen, M. Biermann, A. Molven, H. Sorbye, E. McCormack, M. Postema, O.H. Gilja, A human clinical trial using ultrasound and microbubbles to enhance gemcitabine treatment of inoperable pancreatic cancer, J. Control. Release 243 (2016) 172–181.

[7] Y. Wang, Y. Li, K. Yan, L. Shen, W. Yang, J. Gong, K. Ding, Clinical study of ultrasound and microbubbles for enhancing chemotherapeutic sensitivity of malignant tumors in digestive system, Chin. J. Cancer Res. 30 (2018) 553–563.

[8] N. Saharkhiz, H. Koruk, J.J. Choi, The effects of ultrasound parameters and microbubble concentration on acoustic particle palpation, J. Acoust. Soc. Am. 144 (2018) 796–805.

[9] S. Khalili, M. Mahdi, Numerical analyses of nonlinear behavior of microbubble contrast agents in ultrasound field and effective parameters, J. Acoust. Soc. Am. 143 (2018) 2111–2118.

[10] P. Qin, L. Xu, T. Han, L.F. Du, A.C.H. Yu, Effect of non-acoustic parameters on heterogeneous sonoporation mediated by single-pulse ultrasound and microbubbles, Ultrason. Sonochem. 31 (2016) 107–115.

[11] S. Behnia, M. Yahyavi, R. Habibpourbisafar, Association schemes perspective of microbubble cluster in ultrasonic fields, Ultrason. Sonochem. 44 (2018) 45–52.

[12] F. Dzaharudin, A. Ooi, R. Manasseh, Effects of boundary proximity on monodispersed microbubbles in ultrasonic fields, J. Sound Vib. 410 (2017) 330–343.

[13] M. Postema, G. Schmitz, Ultrasonic bubbles in medicine: influence of the shell, Ultrason. Sonochem. 14 (2007) 438–444.

[14] A.A. Doinikov, A. Bouakaz, Review of shell models for contrast agent microbubbles, IEEE Trans. Ultrason. Ferroelectr. Freq. Control 58 (2011) 981–993.

[15] P.F. Fan, D.X. Yang, J. Wu, Y.Y. Yang, X.S. Guo, J. Tu, D. Zhang, Cell-cycle-dependences of membrane permeability and viability observed for HeLa cells undergoing multi-bubble-cell interactions, Ultrason. Sonochem. 53 (2019) 178–186.

[16] P.F. Fan, Y. Zhang, X.S. Guo, C.L. Cai, M.C. Wang, D.X. Yang, Y.R. Li, J. Tu, L.A. Crum, J.R. Wu, D. Zhang, Cell-cycle-specific cellular responses to sonoporation, Theranostics 7 (2017) 4894–4908.

[17] M. Darnell, A. O'Neil, A. Mao, L. Gu, L.L. Rubin, D.J. Mooney, Material microenvironmental properties couple to induce distinct transcriptional programs in mammalian stem cells, Proc. Natl. Acad. Sci. U.S.A. 115 (2018) E8368–E8377.

[18] G. Brusatin, T. Panciera, A. Gandin, A. Citron, S. Piccolo, Biomaterials and engineered microenvironments to control YAP/TAZ-dependent cell behaviour, Nat. Mater. 17 (2018) 1063–1075.

[19] Y. Ni, M.Y.M. Chiang, Cell morphology and migration linked to substrate rigidity, Soft Matter 3 (2007) 1285–1292.

[20] M.Y. Ali, C.Y. Chuang, M.T.A. Saif, Reprogramming cellular phenotype by soft collagen gels, Soft Matter 10 (2014) 8829–8837.

[21] S.C. Bu, R. Kuijer, R.J. van der Worp, S.M. van Putten, O. Wouters, X.R. Li, J.M.M. Hooymans, L.I. Los, Substrate elastic modulus regulates the morphology, focal adhesions, and alpha-smooth muscle actin expression of retinal muller cells, Invest. Ophth. Vis. Sci. 56 (2015) 5974–5982.

[22] S.Y. Chen, J.S. Lin, B.C. Yang, Modulation of tumor cell stiffness and migration by type IV collagen through direct activation of integrin signaling pathway, Arch. Biochem. Biophys. 555 (2014) 1–8.

[23] K. Mollaeian, Y. Liu, S.Y. Bi, Y.F. Wang, J. Ren, M. Lu, Nonlinear cellular mechanical behavior adaptation to substrate mechanics identified by atomic force microscope, Int. J. Mol. Sci. 19 (2018).

[24] R.S. Stowers, A. Shcherbina, J. Israeli, J.J. Gruber, J. Chang, S. Nam, A. Rabiee, M.N. Teruel, M.P. Snyder, A. Kundaje, O. Chaudhuri, Matrix stiffness induces a tumorigenic phenotype in mammary epithelium through changes in chromatin accessibility, Nat. Biomed. Eng. (2019).

[25] K.R. Levental, H.M. Yu, L. Kass, J.N. Lakins, M. Egeblad, J.T. Erler, S.F.T. Fong, K. Csiszar, A. Giaccia, W. Weninger, M. Yamauchi, D.L. Gasser, V.M. Weaver, Matrix crosslinking forces tumor progression by enhancing integrin signaling, Cell 139 (2009) 891–906.

[26] A.J. Engler, S. Sen, H.L. Sweeney, D.E. Discher, Matrix elasticity directs stem cell lineage specification, Cell 126 (2006) 677–689.

[27] J. Fu, Y.K. Wang, M.T. Yang, R.A. Desai, X. Yu, Z. Liu, C.S. Chen, Mechanical regulation of cell function with geometrically modulated elastomeric substrates, Nat. Methods 7 (2010) 733–736.

[28] M. Versaevel, T. Grevesse, M. Riaz, J. Lantoine, S. Gabriele, Micropatterning hydroxy-PAAm hydrogels and Sylgard 184 silicone elastomers with tunable elastic moduli, Methods Cell Biol. 121 (2014) 33–48.

[29] B. Helfield, X. Chen, S.C. Watkins, F.S. Villanueva, Biophysical insight into mechanisms of sonoporation, Proc. Natl. Acad. Sci. U.S.A. 113 (2016) 9983–9988.

[30] N. Rong, H. Zhou, R. Liu, Y. Wang, Z. Fan, Ultrasound and microbubble mediated plasmid DNA uptake: a fast, global and multi-mechanisms involved process, J. Control. Release 273 (2018) 40–50.

[31] N. Kudo, K. Okada, K. Yamamoto, Sonoporation by single-shot pulsed ultrasound with microbubbles adjacent to cells, Biophys. J. 96 (2009) 4866–4876.

[32] J.R. Tse, A.J. Engler, Preparation of hydrogel substrates with tunable mechanical properties, Curr. Protoc. Cell Biol. (2010) (Chapter 10 Unit 10 16).

[33] P. Getreuer, Chan-Vese segmentation, Image Process. On Line 2 (2012) 214–224.

[34] K. Ferrara, R. Pollard, M. Borden, Ultrasound microbubble contrast agents: fundamentals and application to gene and drug delivery, Annu. Rev. Biomed. Eng. 9 (2007) 415–447.

[35] A.J. Jimenez, P. Maiuri, J. Lafaurie-Janvore, S. Divoux, M. Piel, F. Perez, ESCRT machinery is required for plasma membrane repair, Science 343 (2014) 986-+.

[36] F. Liu, Y. Gao, H. Li, S. Sun, Interaction of propidium iodide with graphene oxide and its application for live cell staining, Carbon 71 (2014) 190–195.

[37] B. Pontes, Y. Ayala, A.C. Fonseca, L.F. Romao, R.F. Amaral, L.T. Salgado, F.R. Lima, M. Farina, N.B. Viana, V. Moura-Neto, H.M. Nussenzveig, Membrane elastic properties and cell function, PLoS One 8 (2013) e67708.

[38] A.R.N. Ramakrishnan, David M. Eckmann, Portnovo Ayyaswamy, Tobias Baumgart, Thomas Pucadyil, Shivprasad Patil, Valerie M. Weaver, Ravi Radhakrishnan, Excess area dependent scaling behavior of nano-sized membrane tethers, Phys. Biol. (2017) 1–27.

[39] J. Wu, Theoretical study on shear stress generated by microstreaming surrounding contrast agents attached to living cells, Ultrasound Med. Biol. 28 (2002) 125–129.

[40] X. Chen, J. Wang, M. Versluis, N. de Jong, F.S. Villanueva, Ultra-fast bright field and fluorescence imaging of the dynamics of micrometer-sized objects, Rev. Sci. Instrum. 84 (2013) 063701.

[41] S.F. Chang, J. Guo, J.C. Sun, S.Y. Zhu, Y. Yan, Y. Zhu, M. Li, Z.G. Wang, R.X. Xu, Targeted microbubbles for ultrasound mediated gene transfection and apoptosis induction in ovarian cancer cells, Ultrason. Sonochem. 20 (2013) 171–179.

[42] K. Kooiman, T. van Rooij, B. Qin, F. Mastik, H.J. Vos, M. Versluis, A.L. Klibanov, N. de Jong, F.S. Villanueva, X. Chen, Focal areas of increased lipid concentration on the coating of microbubbles during short tone-burst ultrasound insonification, PLoS One 12 (2017) e0180747.

[43] K. Kooiman, T.J.A. Kokhuis, T. van Rooij, I. Skachkov, A. Nigg, J.G. Bosch, A.F.W. van der Steen, W.A. van Cappellen, N. de Jong, DSPC or DPPC as main shell component influences ligand distribution and binding area of lipid-coated targeted microbubbles, Eur. J. Lipid Sci. Technol. 116 (2014) 1217–1227.

[44] N. Huebsch, P.R. Arany, A.S. Mao, D. Shvartsman, O.A. Ali, S.A. Bencherif, J. Rivera-Feliciano, D.J. Mooney, Harnessing traction-mediated manipulation of the cell/matrix interface to control stem-cell fate, Nat. Mater. 9 (2010) 518–526.

[45] J. Du, X. Chen, X. Liang, G. Zhang, J. Xu, L. He, Q. Zhan, X.Q. Feng, S. Chien, C. Yang, Integrin activation and internalization on soft ECM as a mechanism of induction of stem cell differentiation by ECM elasticity, Proc. Natl. Acad. Sci. U.S.A. 108 (2011) 9466–9471.

[46] J.L. Brugnano, A. Panitch, Matrix stiffness affects endocytic uptake of MK2-Inhibitor peptides, PLoS One 9 (2014).

[47] J. Li, H.R. Chen, Y. Xu, J.L. Hu, F.Q. Xie, C. Yang, Integrin endocytosis on elastic substrates mediates mechanosensing, J. Biomech. 49 (2016) 2644–2654.

[48] S. Asano, S. Ito, K. Takahashi, K. Furuya, M. Kondo, M. Sokabe, Y. Hasegawa, Matrix stiffness regulates migration of human lung fibroblasts, Physiol. Rep. 5 (2017).

[49] H.J. Vos, B. Dollet, M. Versluis, N. de Jong, Nonspherical shape oscillations of coated microbubbles in contact with a wall, Ultrasound Med. Biol. 37 (2011) 935–948.

[50] H.J. Vos, B. Dollet, J.G. Bosch, M. Versluis, N. de Jong, Nonspherical vibrations of microbubbles in contact with a wall: a pilot study at low mechanical index, Ultrasound Med. Biol. 34 (2008) 685–688.

[51] J. Collis, R. Manasseh, P. Liovic, P. Tho, A. Ooi, K. Petkovic-Duran, Y.G. Zhu, Cavitation microstreaming and stress fields created by microbubbles, Ultrasonics 50 (2010) 273–279.

[52] S.W. Ohl, E. Klaseboer, B.C. Khoo, The dynamics of a non-equilibrium bubble near bio-materials, Phys. Med. Biol. 54 (2009) 6313–6336.

[53] J. Cowley, S. McGinty, A mathematical model of sonoporation using a liquid-crystalline shelled microbubble, Ultrasonics 96 (2019) 214–219.

[54] L. Lee, F. Cavalieri, M. Ashokkumar, Exploring new applications of lysozyme-shelled microbubbles, Langmuir 35 (2019) 9997–10006.

[55] C.J. Slagle, D.H. Thamm, E.K. Randall, M.A. Borden, Click conjugation of cloaked peptide ligands to microbubbles, Bioconjug. Chem. 29 (2018) 1534–1543.